Journal of Energy Storage 34 (2021) 102133

Contents lists available at ScienceDirect

Journal of Energy Storage

journal homepage: www.elsevier.com/locate/est

Temperature estimation from current and voltage measurements in lithium-ion battery systems

P. Wang [a,c,*], L. Yang [c], H. Wang [c], D.M. Tartakovsky [b], S. Onori [b,**]

[a] School of Integrated Circuit Science and Engineering & Beijing Advanced Innovation Center for Big Data and Brain Computing, Beihang University, 100191, China

[b] Department of Energy Resources Engineering, Stanford University, CA 94305, USA

[c] LMIB & School of Mathematical Sciences, Beihang University, 100191, China

ARTICLE INFO

Keywords:
Lithium-ion battery
Temperature estimation
Electrochemical modeling
Ensemble Kalman filter

ABSTRACT

Performance and safety of lithium-ion batteries depend on the ability to efficiently estimate their temperature during charge/discharge operations. We propose a novel algorithm to infer temperature in cylindrical lithium-ion battery cells from measurements of current and terminal voltage. Our approach employs a dual ensemble Kalman filter, which incorporates the enhanced single-particle dynamics to relate terminal voltage to battery temperature and Li-ion concentration. The numerical results and experimental validation from LGChem $LiNiMnCoO_2$ battery (INR21700 M50) cell data demonstrate the method's ability to estimate temperature at various charge/discharge C-rates.

1. Introduction

Lithium-ion battery (LIB) systems are widely used in modern electronic devices. Their reliability and safety are of crucial importance for sustainable development and successful transition to carbon-neutral energy economy. However, safety concerns, mainly due to thermal runaway, hinder large-scale LIB utilization for these purposes. Limiting temperature of LIBs to a restricted window of operation is also important for their longevity and satisfactory performance [1]. Practical limitations preclude direct measurement of temperature of LIB cells within a pack, and accurate temperature estimation from readily available sensors (e.g., current and terminal voltage) remains elusive.

Electrochemical models of LIB systems rely on a number of simplifying assumptions whose veracity is hard to ascertain a priori. For example, the single-particle model (SPM) [2] ignores concentration gradients in the electrolyte (a well-mixed assumption) and approximates the solid phases in both electrodes by spherical particles; it fails to accurately model the terminal voltage at high charge/discharge C-rates. The enhanced SPM model (eSPM) accounts for electrolyte dynamics, yielding improved performance at high C-rates [3,4]. More complex models, e.g., [5–7], incorporate additional physics, but are computationally prohibitive when used either for sampling-based parameter/state estimation or in micro-controllers of battery management systems.

To account for thermal phenomena in batteries, such electrochemical models are supplemented with an energy conservation equation, in which Li ion (Li^+) concentration affects the rate of heat generation. Depending on whether the well-mixed assumption is invoked, the resulting electrochemical–thermal models can be subdivided into lumped (averaged in space) [1,8] and spatially distributed [9–11]. Such electrochemical–thermal models have been used for state of charge and temperature estimation in battery management systems. The experimental validation of thermal models aimed at predicting core temperature is challenging and can pose safety hazards, as it requires a battery to be drilled in order to insert a thermocouple into the cell, in the case of cylindrical cells.

These practical considerations make the ability to estimate the core temperature from existing sensor layouts an appealing objective, which we tackle in this study. Prediction of a battery model, and its use for indirect measurements of battery temperature, are inherently uncertain due to a large number of unknown (fitting) parameters, ambient operating conditions, and sparse sensing [12]. This uncertainty is typically quantified probabilistically by treating uncertain model inputs and outputs as random variables and random processes. The probabilistic framework replaces the inference of a unique parameter value and a unique model prediction with identification of their (joint) probability density functions [13].

* Correspondence to: Beihang University, 37 Xueyuan Road, Beijing, 100191, China.
** Corresponding author.
E-mail addresses: wang.peng@buaa.edu.cn (P. Wang), sonori@stanford.edu (S. Onori).

https://doi.org/10.1016/j.est.2020.102133
Received 24 September 2020; Received in revised form 24 November 2020; Accepted 25 November 2020
Available online 15 December 2020

Nomenclature

j	Index, $j = n$ for anode, $j = p$ for cathode
A	Cell cross-sectional area [m^2]
$c_{s,j}^{max}$	Maximum electrode concentration [mol/m^3]
D_e	Electrolyte phase diffusion [m^2/s]
$C_{e,i}^{in}$	Initial concentration in electrolyte [mol/m^3]
$D_{s,j}^{ref}$	Reference solid phase diffusion [m^2/s]
$E_{D,j}^{act}$	Activation energy for solid phase diffusion in electrode j
$E_{k,j}^{act}$	Activation energy for reaction in electrode j
F	Faraday's constant [C/mol]
k_j^{ref}	Electrode reaction rate constant [$m^{2.5}/s\ mol^{0.5}$]
L_j	Electrode thickness [m]
L_s	Separator thickness [m]
R	Lumped resistance [Ω]
R_g	Universal gas constant [J/mol K]
R_j	Electrode particle radius [m]
t_0^+	Transference number
T_{ref}	Reference temperature [°C]
α_{cell}	Electrode transfer coefficient
ε_j	Electrode active volume fraction of solid phase
$\theta_{j,100\%}$	Reference stoichiometry ratio at 100% SOC
$\theta_{j,0\%}$	Reference stoichiometry ratio at 0% SOC
ω_i	Porosity of anode, cathode, and separator (i = n, p, S)

When combined with sensor measurements, the latter task can be accomplished via sampling-based approaches to data assimilation, such as extended Kalman filter [10]. The reliance on such generalizations of Kalman filter is necessary because the relationship between temperature and the measurable quantities is highly nonlinear in the battery models used and, hence, temperature is highly non-Gaussian. Alternatively, one could sacrifice model veracity by assuming a linear relationship between temperature and the observables in order to use standard Kalman filter [14], but this – the use of an oversimplified model – might lead to erroneous predictions.

Technical contribution and novelty. Temperature has a significant impact on the performance, safety and cycle lifetime of LIBs. Accurate estimation of available charge and energy during short- and long-term operation as well as detection of safety-hindering events are possible only through continuous battery temperature monitoring. Our contribution to the state-of-the-art in estimation of the temperature of LIBs is fourfold. First, our approach utilizes readily available on-board measurements of terminal voltage and current to estimate the temperature. Second, our reliance on a relatively high-fidelity electrochemical model, based on the experimentally validated eSPM, enables us to estimate the battery cell temperature at a wide range of C-rates. Third, we rely on dual ensemble Kalman filter to assimilate measurements of terminal voltage into this complex nonlinear model. Finally, we provide validation of our model predictions by using experimental battery data collected at a different temperature than that used for model calibration.

The remainder of this paper is organized as follows. In Section 2, we formulate the problem and its mathematical conceptualization via the eSPM. Section 3 contains both a description of our general methodology for indirect measurements of the temperature of LIBs and the numerical algorithm for its implementation. In Section 4, we validate our methodology by using experimental data for LGChem $LiNiMnCoO_2$ battery (INR21700 M50). The key conclusions drawn from this study are collated in Section 5.

2. Electrochemical model

LIB cells consist of five major parts: positive electrode (cathode), negative electrode (anode), electrolyte, separator and current collectors (Fig. 1). The two electrodes and the separator have a thickness of L_p, L_n, and L_S, respectively. The cathode is typically a metal oxide ($LiMO_2$), whereas low-cost graphite (C_6) is widely used as anode material due to low electrode potential [15].

The electrolyte is a salt, generally hexafluorophosphate ($LiPF_6$), dissolved in an organic solvent that acts as a transport medium allowing migration of Li^+ between the two electrodes. The electrochemical reactions in a Li-ion cell involve Li^+ moving in and out of the electrodes via intercalation (insertion) and deintercalation (extraction) process, while electrons travel through an external load producing work.

During discharge, an oxidation reaction at the anode produces positively charged Li ions (Li^+) and negatively charged electrons (e^-). This process is described by the anodic half-reaction,

$$Li_yC_6 \longrightarrow yLi^+ + ye^- + C_6. \tag{1a}$$

The Li^+ ions are subsequently transported through the electrolyte and the separator towards the cathode. The electrons pass through the external circuit before reconnecting to the cathode, which undergoes reduction, while the migrated Li^+ ions are intercalated into the cathode. This phenomenon is described by the cathodic half-reaction,

$$Li_{(1-y)}MO_2 + yLi^+ + ye^- \longrightarrow LiMO_2. \tag{1b}$$

During charging, the cathode undergoes oxidation and the anode undergoes reduction [16].

2.1. Enhanced single-particle model for Li^+ concentration

We use the eSPM from [4] as a modeling platform to develop the observer. The eSPM describes diffusion of Li^+ in the cathode, anode and electrolyte of a LIB. The eSPM represents the solid material in each electrode as a spherical particle subjected to a uniform electrical current. Inside of each electrode particle with radius R_j (j = n and p), the Li^+ concentration, $c_{s,j}(r,t)$ with j = n and p, obeys Fick's law of diffusion [3],

$$\frac{\partial c_{s,j}}{\partial t} = \frac{D_{s,j}}{r^2}\frac{\partial}{\partial r}\left[r^2\frac{\partial c_{s,j}}{\partial r}\right], \qquad 0 < r < R_j, \quad t > 0, \quad j = \text{n, p}; \tag{2}$$

and boundary conditions at the sphere's center ($r = 0$) and surface ($r = R_j$),

$$\frac{\partial c_{s,j}}{\partial r}(0,t) = 0, \qquad -D_{s,j}\frac{\partial c_{s,j}}{\partial r}(R_j,t) = \frac{J_j}{F} = \frac{I}{a_j A L_j F}. \tag{3}$$

Here, t [s] denotes time, r [m] is the radial coordinate, F is the Faraday constant, and J_j [A m^{-2}] is the intercalation current density at each electrode. The latter is defined as the input current I [A] divided by the specific interfacial surface area a_j [m^{-1}], the cross-sectional area A [m^2] and the electrode thickness L_j [m]. In our case, $a_j = 3\varepsilon_j/R_j$, where ε_j is the active volume fraction of solid phase [16, Section 3.3.2]. The solid-phase diffusion coefficients $D_{s,j}$ [m^2 s^{-1}] and reaction rate constants $k_{s,j}$ for each electrode have an Arrhenius-type dependence on temperature T [17],

$$D_{s,j} = D_{s,j}^{ref}\exp\left[\frac{E_{D,j}^{act}}{R_g}\left(\frac{1}{T_{ref}} - \frac{1}{T}\right)\right], \tag{4a}$$

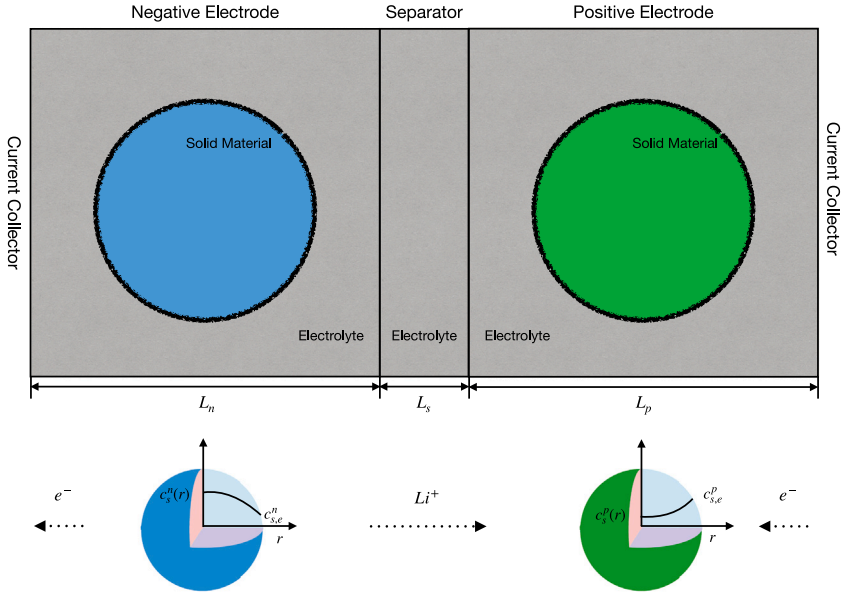

Fig. 1. A schematic diagram of the macroscopic (l-direction) cell model with coupled microscopic (r-direction) solid-diffusion model.

$$k_{s,j} = k_{s,j}^{\mathrm{ref}} \exp\left[\frac{E_{k,j}^{\mathrm{act}}}{R_g}\left(\frac{1}{T_{\mathrm{ref}}} - \frac{1}{T}\right)\right], \tag{4b}$$

where $D_{s,j}^{\mathrm{ref}}$, $k_{s,j}^{\mathrm{ref}}$ and T_{ref} denote the reference values for the diffusion coefficients, reaction rate constants and temperature, respectively; $E_{D,j}^{\mathrm{act}}$ and $E_{k,j}^{\mathrm{act}}$ are the activation energy; and R_g is the universal gas constant.

The Li^+ concentration in the electrolyte phase, $c_{e,i}(x,t)$, is governed by the Planck–Nernst equations,

$$\omega_i \frac{\partial c_{e,i}}{\partial t} = \frac{\partial}{\partial x}\left(D_{e,i}^{\mathrm{eff}} \frac{\partial c_{e,i}}{\partial x}\right) + (1 - t_0^+)\frac{a_i J_i}{F}, \qquad i = \mathrm{n,p,S}, \tag{5}$$

where x is the Cartesian coordinate along the thickness, L, of the cell; ω_i is porosity of the negative (i = n) and positive (i = p) electrodes and the separator (i = S); t_0^+ is the transference number; the exchange current density at the separator is $J_S(t) = 0$; and the effective diffusion coefficients $D_{e,i}^{\mathrm{eff}}$ are assumed to follow the concentration-dependent Bruggeman relation [3],

$$D_{e,i}^{\mathrm{eff}} \approx (\alpha_1 c_{e,i} + \alpha_2)\omega_i^{1.5} \quad \text{with} \quad \alpha_1 = -1.17\times10^{-13}, \quad \alpha_2 = 3.97\times10^{-10}. \tag{6}$$

Eq. (5) are defined on the segments $x \in (0, L_n)$, $(L_n, L_n + L_S)$ and $(L_n + L_S, L = L_n + L_S + L_p)$ representing, the anode, the separator and the cathode, respectively. The external (impermeable) boundary conditions,

$$\frac{\partial c_{e,n}}{\partial x}(0,t) = \frac{\partial c_{e,p}}{\partial x}(L,t) = 0, \tag{7a}$$

are supplemented with continuity conditions at the anode–separator interface, $x = L_n$,

$$c_{e,n}(L_n,t) = c_{e,S}(L_n,t), \qquad D_{e,n}^{\mathrm{eff}}\frac{\partial c_{e,n}}{\partial x}(L_n,t) = D_{e,S}^{\mathrm{eff}}\frac{\partial c_{e,S}}{\partial x}(L_n,t), \tag{7b}$$

and at the separator–cathode interface, $x = L_S^n \equiv L_n + L_S$,

$$c_{e,S}(L_S^n,t) = c_{e,p}(L_S^n,t), \qquad D_{e,S}^{\mathrm{eff}}\frac{\partial c_{e,S}}{\partial x}(L_S^n) = D_{e,p}^{\mathrm{eff}}\frac{\partial c_{e,p}}{\partial x}(L_S^n). \tag{7c}$$

Eqs. (2) and (5) are also subject to initial conditions $c_{s,j}(r,0) = c_{s,j}^{\max} \times \theta_{j,100\%}$ with j = n,p and $c_{e,i}(x,0) = C_{e,i}^{\mathrm{in}}$ with i = n,p,S. Here, $\theta_{j,100\%}$ is the electrode stoichiometry ratio at 100% state of charge (SOC) and $C_{e,i}^{\mathrm{in}}$ is the initial concentration of Li^+ in the electrolyte.

2.2. Terminal voltage

The terminal voltage, V, is defined as [2]

$$V = \Delta\Phi_e + \Delta U_{\mathrm{oc}} + \Delta\eta - IR, \tag{8}$$

where $\Delta\Phi_e \equiv \Phi_e(x = L) - \Phi_e(x = 0)$ is the potential difference in the electrolyte phase, ΔU_{oc} is the open circuit potential difference (positive minus negative) between the electrodes, and $\Delta\eta$ is the over-potential difference between the electrodes, and IR is the voltage drop caused by the lumped resistance. An approximate (linearized) analytical solution of (5) gives an expression for the potential difference in the electrolyte [18],

$$\Delta\Phi_e = \tilde{\kappa}^{\mathrm{eff}} \ln\frac{c_{e,p}(L,t)}{c_{e,n}(0,t)} - \frac{I}{2A}\left(\frac{L_n}{\kappa_n^{\mathrm{eff}}} + \frac{2L_s}{\kappa_s^{\mathrm{eff}}} + \frac{L_p}{\kappa_p^{\mathrm{eff}}}\right). \tag{9a}$$

Here, the effective ionic conductivities κ_i^{eff} are estimated empirically [17],

$$\kappa_i^{\mathrm{eff}} = \bar{c}_{e,i}[(-10.5 + 0.074\,T - 6.96\times10^{-5}T^2) + \bar{c}_{e,i}(0.668 - 0.0178\,T - 2.8\times10^{-5}\,T^2) + \bar{c}_{e,i}^2(0.494 - 8.86\times10^{-4}\,T)]^2, \tag{9b}$$

as functions of temperature T and the average Li^+ concentrations at the anode, cathode or separator $\bar{c}_{e,i}$; and

$$\tilde{\kappa}^{\mathrm{eff}} = \frac{2R_gT(1-t_0^+)(\kappa_n^{\mathrm{eff}} + \kappa_s^{\mathrm{eff}} + \kappa_p^{\mathrm{eff}})}{3F}\left\{0.601 - 0.24\sqrt{\bar{c}_e} + 0.982\,[1 - 0.0052(T - 293)]\,\bar{c}_e^{1.5}\right\}. \tag{9c}$$

The open circuit potentials at the two electrodes, U_p and U_n, are functions of temperature, T, and stoichiometric ratios, θ_p and θ_n, at the solid phase [2],

$$\Delta U_{\mathrm{oc}}(T) = U_p(\theta_p,T) - U_n(\theta_n,T), \qquad \theta_j = c_{s,j}(R_j,t)/c_{s,j}^{\max}, \tag{10}$$

where $c_{s,j}^{\max}$ is the theoretical maximum concentration. The difference between the cathode and anode over-potentials is computed from the Butler–Volmer kinetic equation [19], which describes the rate of intercalation and deintercalation of Li^+,

$$\Delta\eta = \eta_p - \eta_n = \frac{2R_gT}{F}\left[\sinh^{-1}\left(\frac{J_p}{2J_{0,p}}\right) - \sinh^{-1}\left(\frac{J_n}{2J_{0,n}}\right)\right], \tag{11a}$$

where

$$J_{0,j} = Fk_{s,j}\sqrt{\bar{c}_e c_{s,j}^{\mathrm{surf}}(c_{s,j}^{\max} - c_{s,j}^{\mathrm{surf}})}, \qquad j = \mathrm{n,p} \tag{11b}$$

is the exchange current density.

3. Methodology for core temperature estimation

We start by describing a numerical scheme used to solve the eSPM (Section 3.1) and then discuss its observability from measurements (Section 3.2). Our approach to data assimilation and a detailed algorithm for its implementation are outlined in Section 3.3.

3.1. Numerical solution of the eSPM

A finite-difference method is employed to approximate the spatial derivatives in the eSPM [4]. The simulation domain $0 \le r \le R_j$ is discretized with M_s+1 nodes, and the boundary-value problem for the Li^+ concentration in the solid phase, (2) and (3), is discretized in space as

$$\frac{\mathrm{d}c_{s,j}^m}{\mathrm{d}t} = \frac{D_{s,j}M_s^2}{R_j^2}\left(\frac{m-1}{m}c_{s,j}^{m-1} - 2c_{s,j}^m + \frac{m+1}{m}c_{s,j}^{m+1}\right), \quad m = 1,\dots,M-1;$$

and

$$c_{s,j}^0 = c_{s,j}^1 \quad \text{and} \quad c_{s,j}^{M_s} = c_{s,j}^{M_s-1} - \frac{R_j I}{D_{s,j}FM_s a_j A L_j}.$$

For the electrolyte phase, the simulation domains $0 \le x \le L_n$, $L_n < x \le L_n+L_S$ and $L_n+L_S < x \le L$ are discretized, respectively, with $M_{e,n}$, $M_{e,S}$ and $M_{e,p}$ nodes. To simplify the presentation, we assume these nodes to be equally distant for all of these subdomains, such that the distance between any two adjacent nodes in the whole simulation domain $0 \le x \le L$ is $\Delta x = L/M_e$, where $M_e = M_{e,n} + M_{e,S} + M_{e,p}$. Then a finite-difference approximation of (5) on the domain $0 \le x \le L$ is

$$\omega_i \frac{\mathrm{d}c_e^k}{\mathrm{d}t} = \alpha_1 \frac{(c_e^{k-1})^2 - c_e^{k-1}c_e^k - (c_e^k)^2 + c_e^k c_e^{k+1}}{(L/M_e)^2} + \alpha_2 \frac{c_e^{k-1} - 2c_e^k + c_e^{k+1}}{(L/M_e)^2} + (1-t_0^+)\frac{a_i J_i}{F}, \quad k = 1,\dots,M_e-1;$$

with the boundary and interfacial conditions (7a)–(7c) taking the form

$$c_e^0 = c_e^1, \qquad c_e^{M_e} = c_e^{M_e-1},$$
$$\omega_n^{1.5}\frac{c_e^{M_{e,n}} - c_e^{M_{e,p}-1}}{L/M_e} = \omega_S^{1.5}\frac{c_e^{M_{e,n}+1} - c_e^{M_{e,n}}}{L/M_e},$$
$$\omega_S^{1.5}\frac{c_e^{M_{e,p}+M_{e,s}} - c_e^{M_{e,p}+M_{e,s}-1}}{L/M_e} = \omega_p^{1.5}\frac{c_e^{M_{e,p}+M_{e,s}+1} - c_e^{M_{e,p}+M_{e,s}}}{L/M_e}.$$

3.2. Observability of Li^+ concentration from terminal voltage

Our goal is to estimate the battery temperature, $T(t)$, from the terminal output voltage $V(t)$ and input current $I(t)$. Let us define the state vector $\mathbf{c} = (c_{s,n}^0,\dots,c_{s,n}^{M_s}, c_{s,p}^0,\dots,c_{s,p}^{M_s}, c_e^0,\dots,c_e^{M_e})^\top \in \mathbb{R}^{2M_s+M_e+3}$ comprising the Li^+ concentration in the anode, cathode and electrolyte. Then, the eSPM and terminal voltage is rewritten as

$$\frac{\mathrm{d}\mathbf{c}}{\mathrm{d}t} = f_m[\mathbf{c}, T, I], \qquad V = g_m[\mathbf{c}, T, I], \tag{12}$$

where $f_m[\cdot]$ is the eSPM (forward) model that predicts the temporal evolution of the system state $\mathbf{c}(t)$, and $g_m[\cdot]$ is the nonlinear operator that calculates V from the concentrations and temperature in accordance with (8).

System observability refers to the ability to estimate $\mathbf{c}$ and T from measurements of the input I and output V. Since the eSPM is highly nonlinear, we investigate local observability by assuming that $T(t)$ varies slightly within a small time window, such that $\mathrm{d}T/\mathrm{d}t = 0$ locally. This assumption is justified by our experimental observations depicted in Fig. 2.

Consider the vector $\mathbf{w} = (\mathbf{c}^\top, T)^\top \in \mathbb{R}^{2M_s+M_e+4}$, then, the eSPM in (12) is reformulated as

$$\frac{\mathrm{d}\mathbf{w}}{\mathrm{d}t} = \mathbf{F}[\mathbf{w}, I]. \tag{13}$$

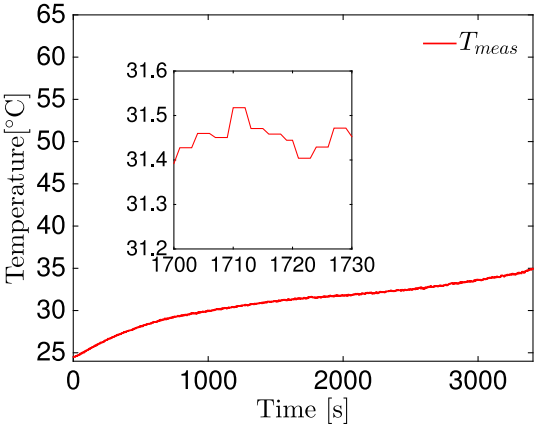

Fig. 2. Experimental data showing the temperature behavior from 1-C rate discharge for the LGChem INR21700 battery cell.

Consider a differentiable manifold M and let X be a differentiable vector field on M. Given a function $f : M \to \mathbb{R}$ and a set $x \in M$, the Lie derivative is defined as $L_X[f] = \partial_x f(x)X(x)$. With this definition, the first $l = 2M_s + M_e + 4 - 1$ Lie derivatives of g_m with respect to $\mathbf{F}$ are

$$\begin{cases} L_{\mathbf{F}}^0[g_m] \equiv g_m \\ L_{\mathbf{F}}^1[g_m] \equiv \nabla g_m \cdot \mathbf{F} \\ L_{\mathbf{F}}^2[g_m] \equiv \nabla(L_{\mathbf{F}}^1[g_m]) \cdot \mathbf{F} \\ \vdots \\ L_{\mathbf{F}}^l[g_m] \equiv L_{\mathbf{F}}\left[L_{\mathbf{F}}^{l-1}[g_m]\right] \end{cases} \tag{14}$$

where

$$\nabla \equiv \left(\frac{\partial}{\partial c_{s,n}^0},\dots,\frac{\partial}{\partial c_e^{M_e}},\frac{\partial}{\partial T}\right).$$

The local observability of this system, at a point $(\mathbf{w}^*, I^*)$, depends on the rank of the matrix [20]

$$\mathbf{O}(\mathbf{w}^*, I^*) = \begin{bmatrix} \nabla(L_F^0[g_m]) \\ \nabla(L_F^1[g_m]) \\ \vdots \\ \nabla(L_F^{l-1}[g_m]) \end{bmatrix}_{\mathbf{w}=\mathbf{w}^*, I=I^*}. \tag{15}$$

Specifically, the system is locally observable if $\mathtt{rank}(\mathbf{O})|_{\mathrm{column}} = 2M_s + M_e + 4$. We verified numerically that this condition holds at different operating points $(\mathbf{w}^*, I^*)$ with $I^* \neq 0$. Therefore, for any unknown initial state, there exists a finite time-step $t_k > 0$, for which the knowledge of the input current I and the output terminal voltage V over the time period $[0, t_k]$ suffices to uniquely determine the initial state.

3.3. Dual ensemble Kalman filter

Various flavors of Kalman filter, e.g., a joint filtering approach [21] or a dual filtering structure [22], can be used to estimate the temperature T. Many of them require the knowledge of the state-parameter matrix, which carries a significant computational cost proportional to the dimensionality of the system. Instead, we deploy the dual ensemble Kalman filter [23] because of its efficiency and ease of implementation.

A key feature of the proposed dual ensemble Kalman filter is the addition of a new equation to describe the quasi-constant change in temperature over the sampling time window between the kth and $(k+1)$st time steps,

$$T_{k+1} = T_k + \epsilon_k^T. \tag{16}$$

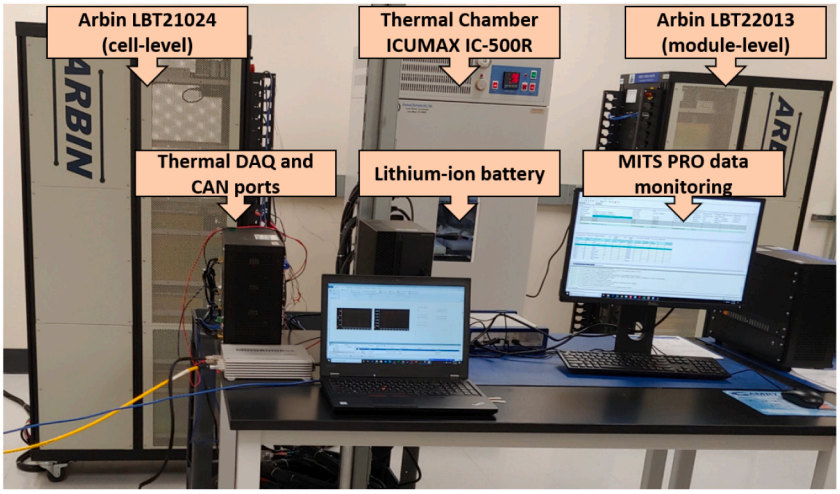

Fig. 3. Experiments were carried out in the Stanford Energy Control laboratory at the Energy Resources Engineering Department, Stanford University.

Here T_k and T_{k+1} are the temperature values at the kth and $(k+1)$st time steps, respectively; and $\epsilon_k^T \in \mathbb{R}$ is a small quantity capturing the temporal change of the temperature over the time window k and $k+1$. We treat ϵ_k^T as a Gaussian random variable with zero mean and variance $\sigma_T^2 \in \mathbb{R}$. By coupling (16) with (12), we obtain a new system for the thus randomized state vector $\mathbf{c}$.

Subsequent assimilation of measurements of current I and terminal voltage V yields an estimate of battery temperature T. Direct measurements of V can be noisy due to errors associated with numerical roundoff and operating conditions. To account for this observation error, we introduce a zero-mean Gaussian process in time, $\epsilon_k^{\mathrm{d}} \in \mathbb{R}$ with variance $\sigma_{\mathrm{d}}^2 \in \mathbb{R}$. Thus, the observed data are modeled as $d_k = V_k^{\mathrm{obs}} + \epsilon_k^{\mathrm{d}}$.

With the model prediction, $\mathbf{w}(t) = (\mathbf{c}^\top, T)^\top$, and observations, $d(t)$, in place, we formulate the state-parameter estimation problem as a filtering problem. Probability of the discrete system state at an arbitrary time step $K \geq 1$ is given by Bayes' theorem,

$$\mathbb{P}(\mathbf{w}_K|\mathcal{D}_K) \propto \mathbb{P}(\mathbf{w}_{K-1}|\mathcal{D}_{K-1})\mathbb{P}(T_K|T_{K-1})\mathbb{P}(\mathbf{c}_K|\mathbf{w}_{K-1})\mathbb{P}(d_K|\mathbf{w}_K), \tag{17}$$

where $\mathcal{D}_K = \{d_k\}_{k=1}^K$ is the data set of terminal voltage measurements collected up to and including the Kth time step. Filtering replaces this computationally expensive Bayesian update with an optimization problem

$$\bar{\mathbf{w}}_K^\star = \underset{\bar{\mathbf{w}}_K}{\operatorname{argmin}} \left\{ \frac{\left[d_K - g_{\mathrm{m}}(\bar{\mathbf{w}}_K, I_K)\right]^2}{\sigma_{\mathrm{d}}^2} + \frac{(\bar{\mathbf{c}}_K - \hat{\mathbf{c}}_K)^2}{\hat{\Sigma}_{\mathbf{c}}^K} + \frac{(\bar{T}_K - \hat{T}_K)^2}{\hat{\Sigma}_T^K} \right\}, \tag{18}$$

where $\bar{\mathbf{w}}_K = (\bar{\mathbf{c}}_K^\top, \bar{T}_K)^\top$ are the posterior means of the system states at the Kth time step; and $\hat{\mathbf{w}}_K = (\hat{\mathbf{c}}_K^\top, \hat{T}_K)^\top$ and $\hat{\Sigma}_{\mathbf{c}}^K$, $\hat{\Sigma}_T^K$ are the prior means and (co)variances predicted by the eSPM (13) at the Kth time step. A pseudo code of the dual ensemble Kalman filter is shown in Algorithm 1.

3.4. Identification of system parameters

The eSPM presented in Section 2 incorporates a large number of parameters, whose values depend on both the battery type and factors such as manufacturing process, duration of past discharge/charge, and working environment. The parameters that have the largest impact on the overall model output are arranged in the vector

$$\Theta = (D_{\mathrm{s,p}}^{\mathrm{ref}}, D_{\mathrm{s,n}}^{\mathrm{ref}}, \theta_{\mathrm{n},100\%}, \theta_{\mathrm{p},100\%}, A, R). \tag{19}$$

These parameters are identified by minimizing the root mean square error between the model-predicted terminal voltage $V(t_k)$ and N_{obs} observations $V_{\mathrm{obs}}(t_k)$,

$$\Theta^\star = \underset{\Theta \in \mathbb{R}^6}{\operatorname{argmin}} \sum_{k=1}^{N_{\mathrm{obs}}} \left| V_{\mathrm{obs}}(t_k) - V(\mathbf{c}_k, T_k, \Theta, t_k) \right|^2. \tag{20}$$

Algorithm 1 Dual state-parameter estimation with ensemble Kalman filter

(i) Initialization, $k = 0$

- Draw N samples for the initial states of Li^+ concentration and temperature, $\mathbf{c}_0^{(n)}, T_0^{(n)}$, $(n = 1, \ldots, N)$, which are taken as uniformly distributed random variables:

$$\mathbf{c}_0 \sim \mathcal{U}(\mathbf{c}_{\min}, \mathbf{c}_{\max}), \qquad T_0 \sim \mathcal{U}(T_{\min}, T_{\max}).$$

(ii) For $k \geq 1$ and for all samples $(n = 1, \ldots, N)$,

(a) Forward prediction of system states:

- Predict temperature and terminal voltage from (12) and (16):

$$\begin{aligned} \hat{T}_{k+1}^{(n)} &= T_k^{(n)} + \epsilon_{k+1}^{\mathrm{T}(n)}, \\ \hat{\mathbf{c}}_{k+1}^{(n)} &= f_{\mathrm{m}}(\mathbf{c}_k^{(n)}, \hat{T}_{k+1}^{(n)}, I_{k+1}), \\ \hat{V}_{k+1}^{(n)} &= g_{\mathrm{m}}(\hat{\mathbf{c}}_{k+1}^{(n)}, \hat{T}_{k+1}^{(n)}, I_{k+1}). \end{aligned}$$

- Perturb the measurements of terminal voltage with data noise:

$$d_{k+1}^{(n)} = V_{k+1}^{\mathrm{obs}} + \epsilon_{k+1}^{\mathrm{d}(n)}.$$

- Compute Kalman gain for temperature, $\mathbf{K}_{k+1}^{\mathrm{tem}}$, and update temperature:

$$\begin{aligned} \mathbf{K}_{k+1}^{\mathrm{tem}} &= \mathrm{Cov}(\hat{T}_{k+1}, \hat{V}_{k+1})[\mathrm{Cov}(\hat{V}_{k+1}, \hat{V}_{k+1}) + \sigma_{\mathrm{d}}^2]^{-1}, \\ T_{k+1}^{(n)} &= \hat{T}_{k+1}^{(n)} + (d_{k+1}^{(n)} - \hat{V}_{k+1}^{(n)})\mathbf{K}_{k+1}^{\mathrm{tem}}. \end{aligned}$$

(b) Update terminal voltage and concentration states:

- Update terminal voltage with temperature

$$\begin{aligned} \hat{\mathbf{c}}_{k+1}^{(n)} &= f_{\mathrm{m}}(\mathbf{c}_k^{(n)}, T_{k+1}^{(n)}, I_{k+1}), \\ V_{k+1}^{(n)} &= g_{\mathrm{m}}(\hat{\mathbf{c}}_{k+1}^{(n)}, T_{k+1}^{(n)}, I_{k+1}). \end{aligned}$$

- Compute Kalman gain matrix for concentration, $\mathbf{K}_{k+1}^{\mathrm{con}}$, and update concentration:

$$\begin{aligned} \mathbf{K}_{k+1}^{\mathrm{con}} &= \mathrm{Cov}(\hat{\mathbf{c}}_{k+1}, V_{k+1})[\mathrm{Cov}(V_{k+1}, V_{k+1}) + \sigma_{\mathrm{d}}^2]^{-1}, \\ \mathbf{c}_{k+1}^{(n)} &= \hat{\mathbf{c}}_{k+1}^{(n)} + (d_{k+1}^{(n)} - V_{k+1}^{(n)})\mathbf{K}_{k+1}^{\mathrm{con}}. \end{aligned}$$

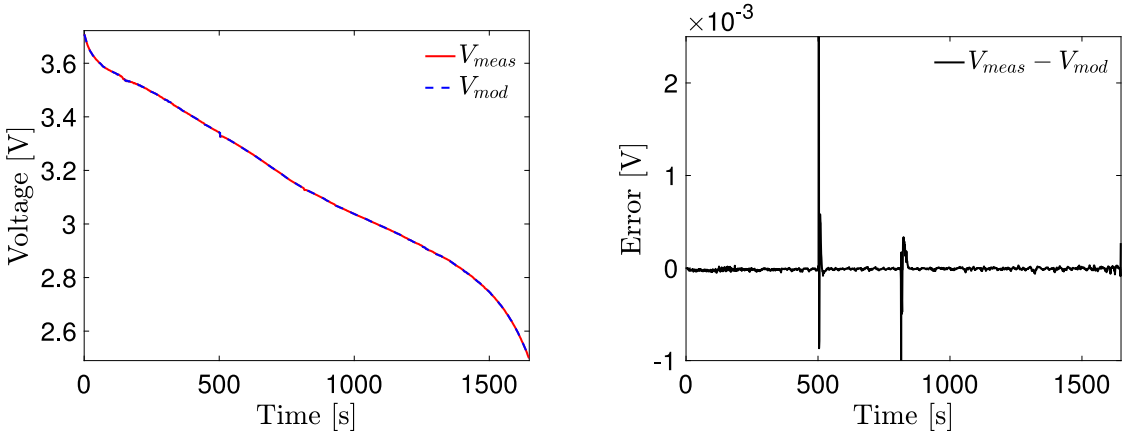

Fig. 4. Left: 2 C-rate discharge profile from measurements (red line) and predicted terminal voltage using identified model parameters (blue dashed line). Right: The discrepancy between the measurement and predicted terminal voltage.

A set of constraints for this minimization problem comes from geometric and physical considerations. The most obvious of these, $A > 0$, $R > 0$ and $0 < \theta_{j,100\%} < 1$, are supplemented with a constraint imposed by the long-time behavior of the Li^+ concentrations in the cathode and anode, $c_{s,j}(r,t)$ ($j = n, p$). Specifically, according to (2), the diffusion time-scale (i.e., the time it takes to reach the equilibrium) in each of the spherical particles is $t' = R_j^2/(\pi D_{s,j})$. Since the time (in seconds) it takes to discharge a battery at 1 C-rate is $t' \in [1, 3600]$, this places a constraint on the solid-phase diffusion coefficient at the two electrodes, $D_{s,j} \leq R_j^2/(\pi t')$ (j=n, p).

In summary, the identification of system parameters in (19) is cast as a quadratic optimization problem (20) subject to the constraints

$$A > 0, \quad R > 0, \quad 0 < \theta_{j,100\%} < 1, \quad 0 < D_{s,j} \leq \frac{R_j^2}{\pi t'} \quad \text{for } j = n, p. \tag{21}$$

4. Experimental setup, results and discussion

The experimental setup used for this work and shown in Fig. 3 includes two Arbin battery testing systems capable of applying diverse current profiles to cells and modules and measure the load current, cell voltage and surface temperature using highly accurate sensors. A thermal chamber is used to conduct temperature controlled experiments and Omega Type-T thermocouples are used to measure the battery surface temperature. The measured current and voltage data from the Arbin are used to identify the eSPM parameters.

Constant current discharge experiments are conducted on LGChem INR21700 M50 cylindrical LIB cells whose chemical composition is lithium nickel manganese cobalt oxide ($LiNiMnCoO_2$ or NMC) for the cathode and mixed graphite and silicon at the anode. The atomic ratio of NMC used in LGChem INR21700 M50 is Ni:Mn:Co:Al = 82.9:5.1:10.6:1.4, and the anode has 90% graphite and 10% $SiO_{0.64}$ in weight percentage [24]. The LIB has a nominal capacity of 4.85 A· h and operates at a nominal voltage 3.63 V with maximum and minimum voltage of 4.20 V and 2.50 V, respectively. The cell was subjected to three input discharged current at 1 C-rate, 2 C-rate and 3 C-rate at a temperature of 25 °C. We measured the terminal voltage and the cell surface temperature.

The finite-difference method described in Section 3.1 is implemented on $M_s = M_e = 31$ nodes. The system of ordinary differential Eqs. (12) is solved with the explicit fourth-order Runge–Kutta method using the MATLAB® solver `ode45`. The vector of model parameters Θ in (19) is obtained as a solution of the constrained optimization problem (Section 3.4) using the MATLAB® prediction error minimization toolbox `pem`. Fig. 4 shows a close agreement between the terminal voltage $V(t)$ predicted with the model upon parameter identification and its observations at the 2 C-rate discharge. The value of identified parameter are reported in Table 1; the fixed parameters are taken from [3,24].

Table 1
Values of the model parameters. The horizontal line separates the fixed parameters from those identified via model calibration at 2 C-rate discharge.

Parameters	Anode	Cathode	Separator
L_j	3.655×10^{-5}	4×10^{-5}	2.5×10^{-5}
D_e	1.5×10^{-10}	1.5×10^{-10}	1.5×10^{-10}
$C_{e,i}^{in}$	1200	1200	1200
ω_i	0.4	0.4	0.4
$\bar{c}_{e,i}$	1200	1200	1200
α_{cell}	0.5	0.5	
t_0^+	0.363	0.363	
$c_{s,j}^{max}$	31080	51830	
R_j	5×10^{-6}	5×10^{-6}	
ε_j	0.662	0.58	
k_j^{ref}	1×10^{-10}	1×10^{-10}	
$E_{D,j}^{act}$	4×10^4	2.5×10^4	
$E_{k,j}^{act}$	3×10^4	3×10^4	
R_g	8.314		
F	96487		
T_{ref}	25		
$D_{s,j}^{ref}$	3.825×10^{-14}	3.196×10^{-14}	
$\theta_{j,100\%}$	0.836	0.375	
A	2.836×10^{-1}		
R	4.967×10^{-2}		

We used the dual ensemble Kalman filter with 20 samples to estimate the LIB temperature, T, from 3408, 1648 and 1027 direct measurements of V for 1, 2 and 3 C-rate discharge, respectively. The measurement error variance is $\sigma_v^2 = 1 \times 10^{-6}$ V^2, and the variance of the temperature model error is $\sigma_T^2 = 0.001$ °C^2. In Fig. 5, the temporal evolutions of temperature T, reconstructed from direct measurements and estimated via the proposed ensemble Kalman filter at 1, 2 and 3 C-rate discharge are shown. In all regimes, the algorithm yields averaged (smoothed) temperature profiles that are in close agreement with the observations. Moreover, in Fig. 5 the prediction errors, i.e., the difference between the observed and predicted values of voltage V are shown for the same C-rates. The maximum error at 2 C-rate discharge reaches 2 °C, whereas its counterparts at the two other rates are merely 0.6 °C. The temperature root mean square error (RMSE) at 1, 2 and 3 C-rate discharge is 0.1085, 0.2550 and 0.3224, respectively.

The results shown demonstrate that the proposed method can effectively forecast the LIB temperature at a constant current. Moreover, it is also applicable to high-rate currents, as discussed in Section 3.3 wherein the current varies with time. Application of our method to discharge/charge cycles with varying ambient temperature is left for future studies. For example, a working cycle of an LIB in an electric

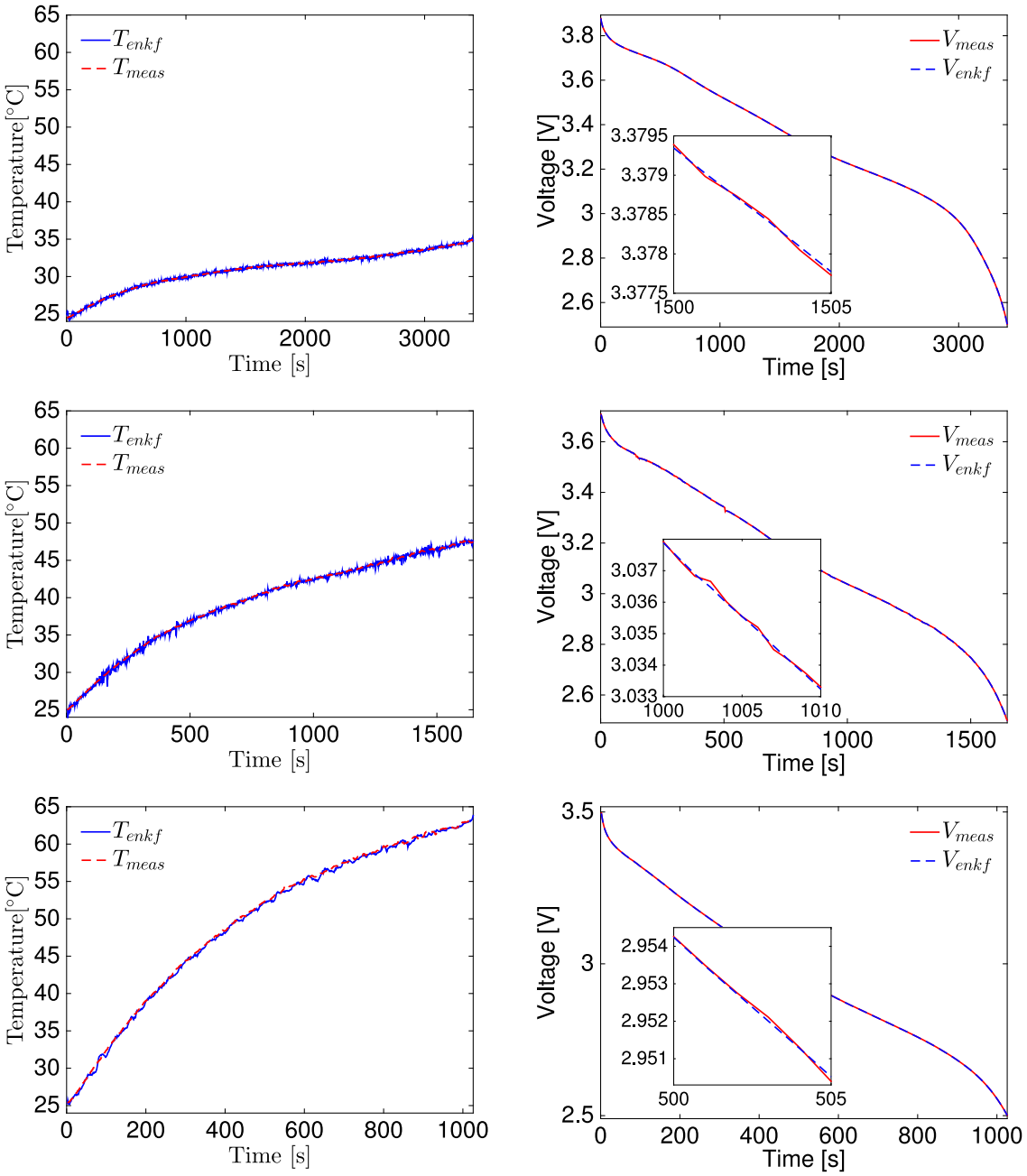

Fig. 5. Left column: Temporal evolution of the LIB temperature $T(t)$, predicted with dual ensemble Kalman filter (solid line) and observed experimentally (dashed line) at 1 C-rate (Top), 2 C-rate (Middle), 3 C-rate (Bottom). The predicted results are averages over 20 realizations. Right column: The corresponding voltage $V(t)$, predicted with dual ensemble Kalman filter (dashed lines) and observed experimentally (solid lines).

vehicle consists of a sequence of charging (regenerative braking) and discharging of the battery. In addition, since the definition of f_m and g_m is general, our method can potentially work for other battery types as long as the state propagation function model is accurate.

5. Summary and conclusions

We proposed a novel algorithm to estimate the temperature of a LIB cell using the currently available on-board current and voltage sensors by means of inversion of the electrochemical dynamics. It uses the enhanced single-particle model to relate the current and terminal voltage to the temperature, and a dual ensemble Kalman filter to assimilate direct measurements of the former into predictions of the latter.

The proposed numerical framework provides accurate estimates of battery temperature, terminal voltage and Li^+ concentration in both the solid phase and the electrolyte, over a wide range of C-rate discharge. Results have been validated against experimental data collected from the LGChem NMC battery cells at the Stanford Energy Control laboratory.

The proposed algorithm can be used in current battery management systems to enhance SOC/SOH estimation while guaranteeing battery safety operation.

Declaration of competing interest

The authors declare that they have no known competing financial interests or personal relationships that could have appeared to influence the work reported in this paper.

Acknowledgments

P. Wang, L. Yang, and H. Wang were supported by the National Key Research and Development Program of China (Grant No. 2017YFB0701700 and 2018YFB0703902). DMT was supported in part by the gift from Total. We thank Anirudh Allam, Ph.D. student at ERE Department, Stanford University, for making the eSPM numerical code from [4] available. Experimental battery data were collected at the Stanford Energy Control Lab, https://onorilab.stanford.edu/research.

References

[1] C. Forgez, D.V. Do, G. Friedrich, M. Morcrette, C. Delacourt, Thermal modeling of a cylindrical LiFePO4/graphite lithium-ion battery, J. Power Sour. 195 (9) (2010) 2961–2968.
[2] M. Guo, G. Sikha, R.E. White, Single-particle model for a lithium-ion cell: Thermal behavior, J. Electrochem. Soc. 158 (2) (2011) A122–A132.
[3] T.R. Tanim, C.D. Rahn, C.-Y. Wang, State of charge estimation of a lithium ion cell based on a temperature dependent and electrolyte enhanced single particle model, Energy 80 (2015) 731–739.
[4] A. Allam, S. Onori, An interconnected observer for concurrent estimation of bulk and surface concentration in the cathode and anode of a lithium-ion battery, IEEE Trans. Ind. Electron. 65 (9) (2018) 7311–7321.
[5] M. Doyle, T. Fuller, J. Newman, Modeling of the Galvanostatic charge and discharge of the lithium/polymer/insertion cell, J. Electrochem. Soc. 140 (6) (1993) 1526–1533.
[6] H. Arunachalam, S. Onori, I. Battiato, On veracity of macroscopic lithium-ion battery models, J. Electrochem. Soc. 162 (10) (2015) A1940–A1951.
[7] X. Zhang, D.M. Tartakovsky, Effective ion diffusion in charged nanoporous materials, J. Electrochem. Soc. 164 (4) (2017) E53–E61.
[8] X. Lin, H.E. Perez, J.B. Siegel, A.G. Stefanopoulou, Y. Li, R.D. Anderson, Y. Ding, M.P. Castanier, Online parameterization of lumped thermal dynamics in cylindrical lithium ion batteries for core temperature estimation and health monitoring, IEEE Trans. Control Syst. Tech. 21 (5) (2012) 1745–1755.
[9] W.B. Gu, C.Y. Wang, Thermal-electrochemical modeling of battery systems, J. Electrochem. Soc. 147 (8) (2000) 2910–2922.
[10] Y. Kim, S. Mohan, J.B. Siegel, A.G. Stefanopoulou, Y. Ding, The estimation of temperature distribution in cylindrical battery cells under unknown cooling conditions, IEEE Trans. Control Syst. Tech. 22 (6) (2014) 2277–2286.
[11] M.V. Morganti, S. Longo, M. Tirovic, C.-Y. Blaise, G. Forostovsky, Multi-scale, electro-thermal model of NMC battery cell, IEEE Trans. Veh. Tech. 68 (11) (2019) 10594–10606.
[12] X. Lin, H.E. Perez, J.B. Siegel, A.G. Stefanopoulou, Robust estimation of battery system temperature distribution under sparse sensing and uncertainty, IEEE Trans. Control Syst. Tech. 28 (3) (2020) 753–765.
[13] D.M. Tartakovsky, P.A. Gremaud, Method of distributions for uncertainty quantification, in: R. Ghanem, D. Higdon, H. Owhadi (Eds.), Handbook of Uncertainty Quantification, Springer, 2015, pp. 1–22.
[14] J. Sun, G. Wei, L. Pei, R. Lu, K. Song, C. Wu, C. Zhu, Online internal temperature estimation for lithium-ion batteries based on Kalman filter, Energies 8 (5) (2015) 4400–4415.
[15] J. Kasnatscheew, T. Placke, B. Streipert, S. Rothermel, R. Wagner, P. Meister, I.C. Laskovic, M. Winter, A tutorial into practical capacity and mass balancing of lithium ion batteries, J. Electrochem. Soc. 164 (12) (2017) A2479.
[16] C.D. Rahn, C.-Y. Wang, Battery System Engineering, John Wiley & Sons, Ltd, 2013.
[17] L.O. Valøen, J.N. Reimers, Transport properties of LiPF6-based Li-ion battery electrolytes, J. Electrochem. Soc. 152 (5) (2005) A882–A891.
[18] E. Prada, D. Di Domenico, Y. Creff, J. Bernard, V. Sauvant-Moynot, F. Huet, Simplified electrochemical and thermal model of LiFePO4-graphite Li-ion batteries for fast charge applications, J. Electrochem. Soc. 159 (9) (2012) A1508–A1519.
[19] Y. Ji, Y. Zhang, C. Wang, Li-ion cell operation at low temperatures, J. Electrochem. Soc. 160 (4) (2013) A636–A649.
[20] R. Hermann, A. Krener, Nonlinear controllability and observability, IEEE Trans. Automat. Control 22 (5) (1977) 728–740.
[21] L. Ljung, Asymptotic behavior of the extended Kalman filter as a parameter estimator for linear systems, IEEE Trans. Automat. Control 24 (1) (1979) 36–50.
[22] E.A. Wan, A.T. Nelson, Dual extended Kalman filter methods, in: Kalman Filtering and Neural Networks, vol. 123, Wiley Online Library, 2001.
[23] H. Moradkhani, S. Sorooshian, H.V. Gupta, P.R. Houser, Dual state–parameter estimation of hydrological models using ensemble Kalman filter, Adv. Water Resour. 28 (2) (2005) 135–147.
[24] C.-H. Chen, F.B. Planella, K. O'Regan, D. Gastol, W.D. Widanage, E. Kendrick, Development of experimental techniques for parameterization of multi-scale lithium-ion battery models, J. Electrochem. Soc. 167 (8) (2020) 080534.